Supporting Information for
"The 2015 M_w7.2 Sarez strike-slip earthquake in the Pamir interior: Response to the underthrusting of India's western promontory"

Sabrina Metzger[1], Bernd Schurr[1], Lothar Ratschbacher[2], Henriette Sudhaus[3], Sofia-Katherina Kufner[1], Tilo Schöne[4], Yong Zhang[5], Mason Perry[6] and Rebecca Bendick[6]

[1]Lithosphere Dynamics, GFZ German Research Centre for Geosciences, Potsdam, Germany
[2]Geologie, TU Bergakademie Freiberg, Freiberg, Germany
[3]Institute of Geosciences, Christian-Albrechts-University, Kiel, Germany
[4]Geodetic Hazard Monitoring, GFZ German Research Centre for Geosciences, Potsdam, Germany
[5]School of Earth and Space Sciences, Peking University, Beijing, China
[6]Department of Geosciences, University of Montana, Missoula, Montana, USA

SAR data processing: Interferometry & amplitude pixel offset estimation

After updating the orbit information using the post-processed, precise orbit ephemerides from the Precise Orbit Determination (POD) for SENTINEL-1A, we debursted and deramped the data. The sub-swaths are stitched together using a lookup table that was created in an iterative co-registration process, where the offsets were estimated based on (1) the topographic information from the digital elevation model of the shuttle radar topography mission (SRTM) [*Farr et al.*, 2007; *Jarvis et al.*, 2008], (2) an iterative estimation of the cross-correlation and (3) a spectral diversity estimation that considers the double difference phase of the burst overlap areas [*Scheiber and Moreira*, 2000]. This extremely precise offset estimation is necessary to oppress phase shifts at the overlap area between bursts and sub-swaths, caused by large Doppler centroid variations due to the acquisition squint angle [*Yague-Martinez et al.*, 2016]. The phase shifts pose a problem particularly in interferometric data with high deformation gradients and should be kept to a minimum, because they could cause unwrapping errors in areas with a high fringe density. From the concatenated and co-registered SAR images we calculated interferograms with a multi-look of 40 in range and 8 in azimuth (corresponding to a pixel size on the ground of ~100 m) and removed the topographic signal estimated from the 90 m SRTM digital elevation elevation model. To

Corresponding author: Sabrina Metzger, `metzger@gfz-potsdam.de`

further increase the coherence we applied an adaptive spectral filter [*Goldstein and Werner*, 1998] with a relatively strong filter exponent of 0.7.

We unwrapped the interferograms using a minimum cost-flow approach and triangulation [*Wegmüller and Werner*, 1997]. In the area close to the surface rupture, unwrapping became difficult because the fringe density exceeds the spatial pixel sampling (*Nyquist* frequency). To prevent unwrapping artifacts, we masked the area closer than 10-20 km to the surface rupture (Figure S2). We corrected the data for any signal contribution due to layered atmosphere by estimating a linear dependency between phase and topography. Not accounted for in this approach is turbulent atmospheric phase signal. In the modeling we consider this spatially correlated data error through data weighting [*Sudhaus and Jónsson*, 2009].

The pixel offsets in range and azimuth direction were estimated using a window width of 100 and 20 respectively, in range and azimuth direction. To account for the curvature of the earth and the orbit height, the azimuth offsets were decreased by 0.9 (to project the apparent pixel size seen from the satellite height to the real size on Earth's surface). The relative quality of the range pixel offsets is much better than of the azimuth pixel offsets. This is explained by the spatial resolution, which is 6 times higher in range (2.3 m) than in azimuth (14.0 m).

GPS data processing: Quantifying the co-seismic offsets

For the 1 Hz GPS data, we estimated the static offset by calculating the mean of 250 samples before and after the earthquake (i. e. after the arrival of the surface waves, Figure S3). As expected, the two furthest stations, AYVA and ASAI, did not record any offset worth mentioning. For the other stations in the Alai valley north of the epicenter we detected offsets on the north component only (Table S2). Station ABRA near the Abramov glacier also yields an offset in the east component, but this station is known to drift over the day due to horizon blocking, therefore we excluded this observation. If the uncertainties of the GPS time-series are included, only high-rate GPS station ALA6 showed a displacement above the detection threshold.

The GPS data of FAYZ and MANM are sampled with 30 seconds. We therefore compared the difference in the daily solution before and after the earthquake as they are calculated with GAMIT/GLOBK [*Herring et al.*, 2010a,b,c]. MANM showed a significant dis-

placement in the east component, the signal of all other data was within the noise level (Table S2).

SAR data subsampling

To reduce computational costs we decreased the number of SAR data points to ~1900 using quad-tree subsampling (Figure S2) [*Jónsson et al.*, 2002]. The azimuthal offsets were subsampled in squares of equal size due to the relatively poor data quality. We estimated the data error for each quad using a statistically-derived covariance function built on the non-deforming part of the SAR data and the full variance-covariance matrix [*Sudhaus and Jónsson*, 2009]. First, we sampled the data to create semi-variograms and covariograms [*Chilés and Delfiner*, 1999]. The data variance is given by the sill and the covariance is fitted using an exponential decay function. We then used this information to calculate the data weight of each point, which is inversely proportional to the sum of its variance and covariances with respect to all other data points. The weights of the different data sets can then directly be compared and used as data weights in the optimization and inversion (Figure S4).

Modeling

Finding the best fault geometry

To be able to best-represent the double-kink-pattern observed in the amplitude pixel offset estimation (Figure 2 in main text) we solved for the best-fit using three rectangular fault segments [*Okada*, 1985] linked at the up-dip end, but otherwise of unconstrained size, location and orientation. Fifty independent simulated annealing optimization runs revealed a couple of stable minima in the model space with comparable misfits, probably because the optimization routine reached its resolution limits. This is nicely illustrated when e.g. the end points of the three connected fault planes are plotted together with amplitude offset data (Figure S6). We chose the best-fit model parameters being the ones providing the lowest misfit.

In order to obtain model parameter uncertainties that account for data uncertainties, we performed additional 500 independent runs with “perturbed” input data, which increased the uncertainties obtained above (Figure S6, S7 and S8). “Perturbed” means that the input data was modified with a random error scaled with the single data errors.

Slip inversion and smoothing constraints

While inverting for slip to best predict the observations d_{obs} we combined the Green's functions G_{slip} with six parameters controlling the phase ambiguities, G_{amb} for potential orbital signals in the two interferograms and a smoothing operator D_{smo} with a weighting factor κ:

$$\begin{bmatrix} d_{\text{obs}} \\ 0 \end{bmatrix} = \begin{bmatrix} G_{\text{slip}} & G_{\text{amb}} \\ \kappa D_{\text{smo}} & 0 \end{bmatrix} \tag{1}$$

The smoothing operator constrains the slip of a patch to be of the same amount as the accumulated slip of all adjacent patches [*Jónsson et al.*, 2002]. For the optimal patch model, we chose a smoothing factor of $\kappa = 30$, based on a trade-off curve between fit and the maximum slip (Figure 5A). For the uniform patch model, we chose a smoothing factor of $\kappa = 90$, based on a trade-off curve between data fit and and roughness [*Jónsson et al.*, 2002] (Figure 5B).

References

Chilés, J.-P., and P. Delfiner (1999), Geostatistics – Modelling spatial uncertainties, *Wiley Series in Probabililty and Statistics*, (John Wiley & Sons Inc., New York), Applied probability and Statistics Section.

Farr, T. G., P. A. Rosen, E. Caro, R. Crippen, R. Duren, S. Hensley, M. Kobrick, M. Paller, E. Rodriguez, L. Roth, D. Seal, S. Shaffer, J. Shimada, J. Umland, M. Werner, M. Osking, D. Burbank, and D. Alsdorf (2007), The shuttle radar topography mission, *Rev. of Geophys.*, *45*(RG2004), doi:10.1029/2005RG000183.

Goldstein, R. M., and C. L. Werner (1998), Radar interferogram filtering for geophysical applications, *Geophys. Res. Lett.*, *25*(21), 4035–4038, doi:10.1029/1998GL900033.

Herring, T. A., R. W. King, and S. C. McClusky (2010a), Introduction to GAMIT/GLOBK, Release 10.4, *Department of Earth, Atmospheric, and Planetary Sciences, Massachusetts Institute of Technology, Cambridge, Massachusetts*.

Herring, T. A., R. W. King, and S. C. McClusky (2010b), GAMIT Reference Manual - GPS Analysis at MIT, Release 10.4, *Department of Earth, Atmospheric, and Planetary Sciences, Massachusetts Institute of Technology, Cambridge, Massachusetts*.

Herring, T. A., R. W. King, and S. C. McClusky (2010c), GLOBK Reference Manual - Global Kalman filter VLBI and GPS analysis program, Release 10.4, *Department of Earth, Atmospheric, and Planetary Sciences, Massachusetts Institute of Technology, Cambridge, Massachusetts*.

Jarvis, A., H. I. Reuter, A. Nelson, and E. Guevara (2008), Hole-filled SRTM for the globe Version 4, available from the CGIAR-CSI SRTM 90m Database, doi: http://srtm.csi.cgiar.org.

Jónsson, S., H. Zebker, P. Segall, and F. Amelung (2002), Fault slip distribution of the 1999 Mw 7.1 Hector Mine, California, earthquake, estimated from satellite radar and GPS measurements, *Bull. Seism. Soc. Am.*, *92*(4), 1377–1389, doi:10.1785/0120000922.

Okada, Y. (1985), Surface deformation due to shear and tensile faults in a half-space, *Bull. Seism. Soc. Am.*, *75*(4), 1135–1154.

Rutte, D., L. Ratschbacher, S. Schneider, K. Stübner, M. A. Stearns, M. A. Gulzar, and B. R. Hacker (2017), Building the Pamir-Tibet Plateau – Crustal stacking, extensional collapse, and lateral extrusion in the Central Pamir: 1. Geometry and kinematics, *Tectonics*, *36*, 342–384, doi:10.1002/2016TC004293.

Sangha, S., G. Peltzer, A. Zhang, L. Meng, C. Lian, P. Lundgren, and E. Fielding (2017), Fault geometry of 2015, Mw7.2 Murghab, Tajikistan earthquake controls rupture propagation: Insights from InSAR and seismological data, *Earth Plan. Sci. Lett.*, *462*, 132–141, doi:10.1016/j.epsl.2017.01.018.

Scheiber, R., and A. Moreira (2000), Coregistration of interferometric SAR images using spectral diversity, *Geoscience and Remote Sensing, IEEE Transactions on*, *38*(5), 2179–2191, doi:10.1109/36.868876.

Strecker, M. R., W. Frisch, M. W. Hamburger, L. Ratschbacher, S. Semiletkin, A. Zamoruyev, and N. Sturchio (1995), Quaternary deformation in the Eastern Pamirs, Tadzhikistan and Kyrgyzstan, *Tectonics*, *14*(5), 1061–1079, doi:10.1029/95TC00927.

Sudhaus, H., and S. Jónsson (2009), Improved source modeling through combined use of InSAR and GPS under consideration of correlated data errors: Application to the June 2000 Kleifarvatn earthquake Iceland, *Geophys. J. Int.*, *176*(2), 389–404, doi:10.1111/j.1365-246X.2008.03989.x.

USGS (2015), M 7.2 - 104km W of Murghob, Tajikistan, *Tech. rep.*, US Geological Survey.

Wegmüller, U., and C. Werner (1997), Gamma SAR processor and interferometry software, *ERS symposium on space at the service of our environment, Florence, Italy*, pp. 1687–

1692.

Yague-Martinez, N., P. Prats-Iraola, F. Rodriguez Gonzalez, R. Brcic, R. Shau, D. Geudtner, M. Eineder, and R. Bamler (2016), Interferometric Processing of Sentinel-1 TOPS Data, *IEEE Trans. Geosc. and Rem. Sens.*, *54*(4), 2220–2234, doi:10.1109/TGRS.2015.2497902.

Table 1. Sentinel-1A SAR data acquisition parameters. $B_\perp$: perpendicular baseline

Acquisition dates	Orbits	Flight mode	$B_\perp$
20151206 – 20151230	8922 / 9272	descending	136 m
20151118 – 20151212	8652 / 9002	ascending	19 m

Table 2. GPS station information, distance to the epicenter, measured static offsets and 1σ-uncertainties for East (E), North (N) and vertical (U) component.

Station	Latitude	Longitude	Distance	Rate	dE [m]	dN [m]	dU [m]	σE [m]	σN [m]	σU [m]
ALA6	72.23272°	39.21072°	121 km	1 s	-	-0.020	-	0.015	0.020	0.045
ALAI	72.16589°	39.52653°	155 km	1 s	-	-0.008	-	0.015	0.020	0.045
SARY	73.19371°	39.70529°	170 km	1 s	-	-0.014	-	0.015	0.020	0.045
ABRA	71.58577°	39.64856°	190 km	1 s	-	-0.010	-	0.015	0.020	0.045
ASAI	76.52096°	40.91782°	440 km	1 s	-	-	-	0.015	0.020	0.045
AYVA	68.02358°	36.97911°	442 km	1 s	-	-	-	0.015	0.020	0.045
MANM	71.6804°	37.5423°	122 km	30 s	-0.010	-0.002	-0.001	0.003	0.002	0.010
FAYZ	70.3434°	37.0733°	250 km	30 s	-0.003	-0.001	0.006	0.003	0.003	0.011

Table 3. Fault geometry used for slip model inversion. The central locations of each fault plane are given in UTM zone 43S. To guarantee capture the full slip pattern in the slip inversion, the segments obtained in the best-fit geometry search were extended from the surface to a depth of 60 km and the outer two segments were elongated to 60 km. The parameters marked with a * are of *Sangha et al.* [2017].

Fault segment	East [km]	North [km]	Length [km]	Strike [°]	Dip [°]	Strike* [°]	Dip* [°]
SW	$313.3^{+0.9}_{-0.0}$	$4239.5^{+1.2}_{-0.0}$	$23.5^{+2.4}_{-0.2}$	$037.4^{+0.1}_{-0.3}$	$87.7\mathrm{NW}^{+1.3}_{-0.8}$	035.4	$89\mathrm{SE}^{+2.3}_{-6.8}$
SW (elongated)	302.2	4225.0	60				
Center	$327.3^{+0.9}_{-0.0}$	$4255.1^{+1.1}_{-0.0}$	$18.5^{+0.2}_{-2.8}$	$047.6^{+2.0}_{-0.0}$	$81.8\mathrm{NW}^{+0.9}_{-3.0}$	054.6	$80\mathrm{NW}^{+9.3}_{-7.2}$
NE	$339.3^{+0.4}_{-0.2}$	$4272.1^{+0.4}_{-0.3}$	$23.8^{+0.9}_{-0.8}$	$025.6^{+0.7}_{-0.6}$	$89.3\mathrm{SE}^{+0.9}_{-1.1}$	030.1	$83\mathrm{NW}^{+8.2}_{-3.5}$
NE (elongated)	347.1	4288.4	60				

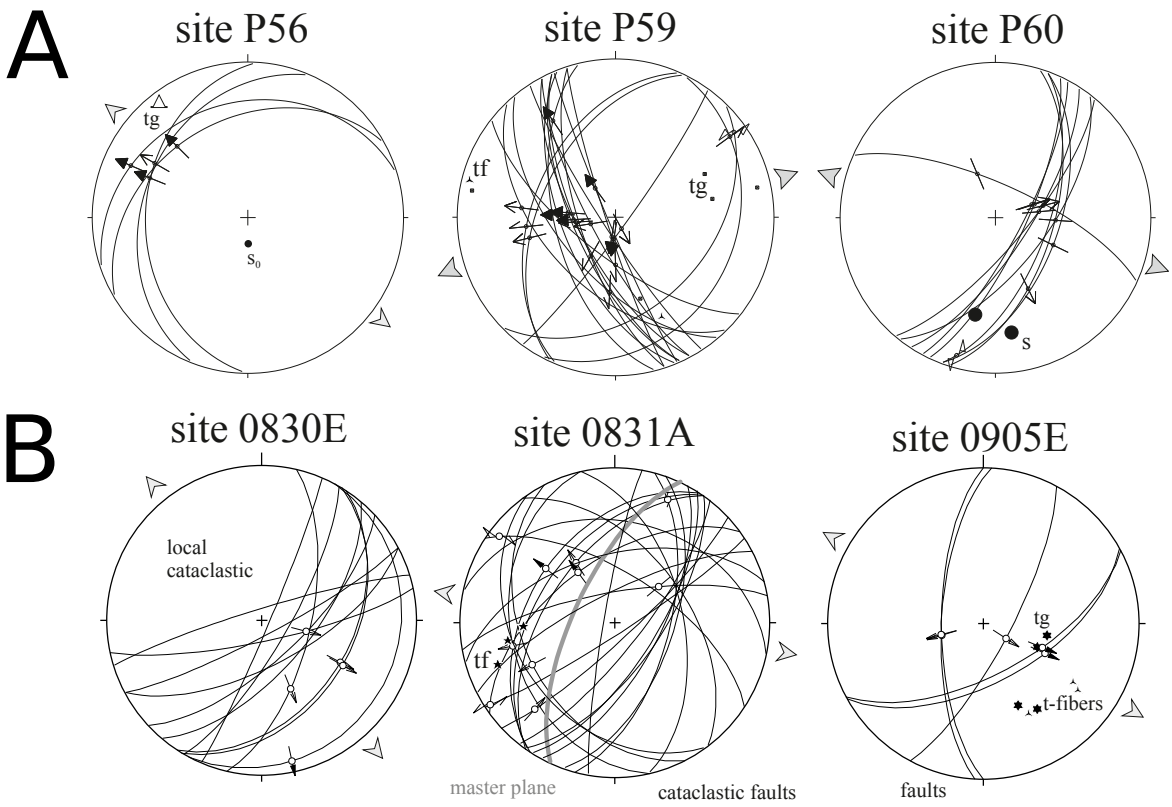

Figure 1. Compilation of published structural data of Late Cenozoic deformation along the northern and central Sarez-Karakul fault system that constrain the overall sinistral-oblique normal slip along the SKFS from the northern segment [*Strecker et al.*, 1995] (A) and the central segment [*Rutte et al.*, 2017] (B). s_0, bedding; s, foliation; tf, tension fracture; tg, tension gash; t-fibers, tension-fibers in gashes; greate circles are faults and arrows give sense of slip of the hanging wall, gray arrows, orientation of the last compressive stress.

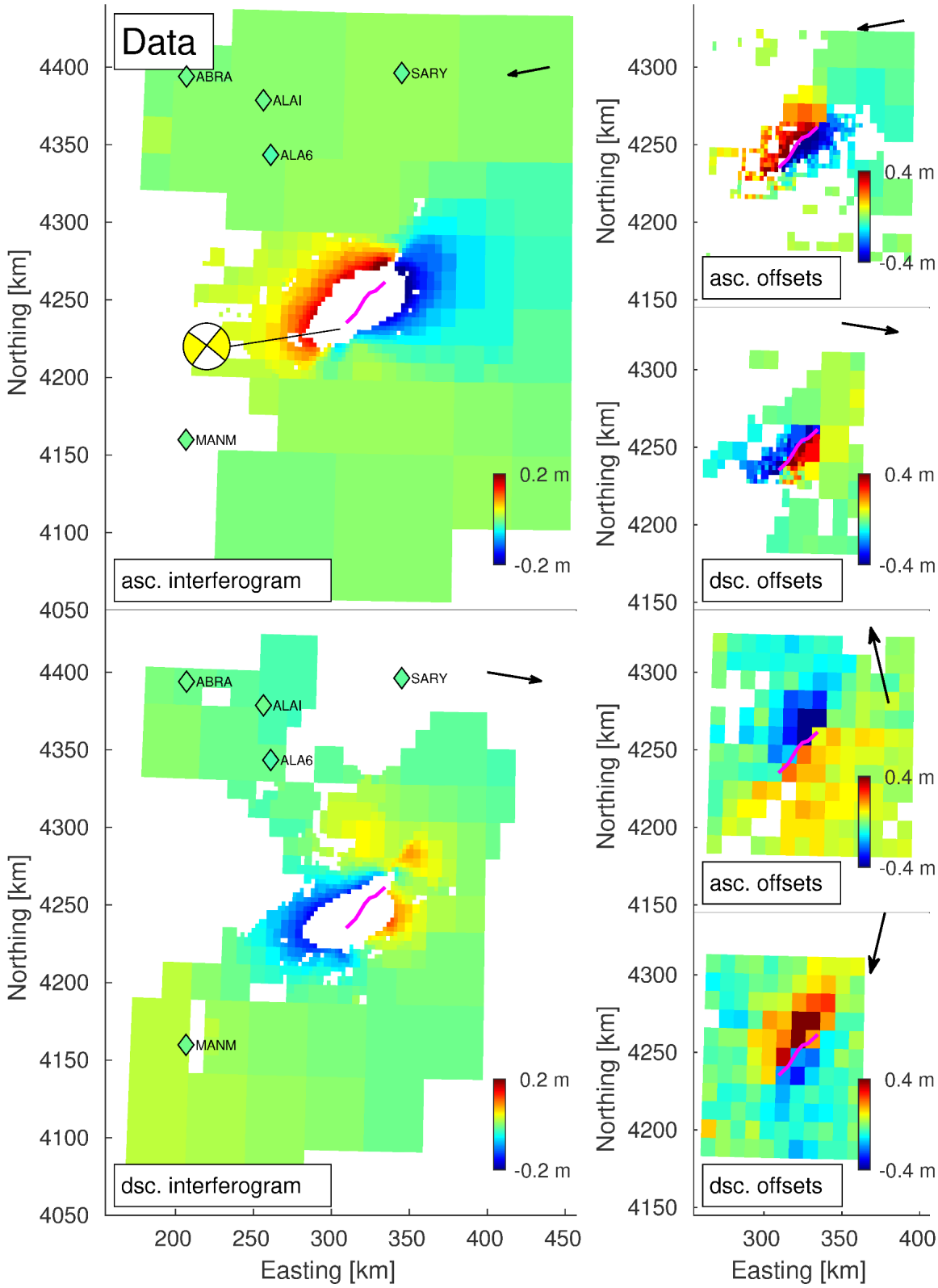

Figure 2. Quad-tree subsampled interferograms and pixel amplitude offsets. The sign change (observed in the amplitude offsets) is outlined in pink, the epicenter marked by the focal mechanism (top left panel, *USGS* [2015]) and the line-of-sight is indicated with a black arrow. Note the different color scale for interferometric and pixel offset data. Geographic coordinates are with respect to UTM zone 43S.

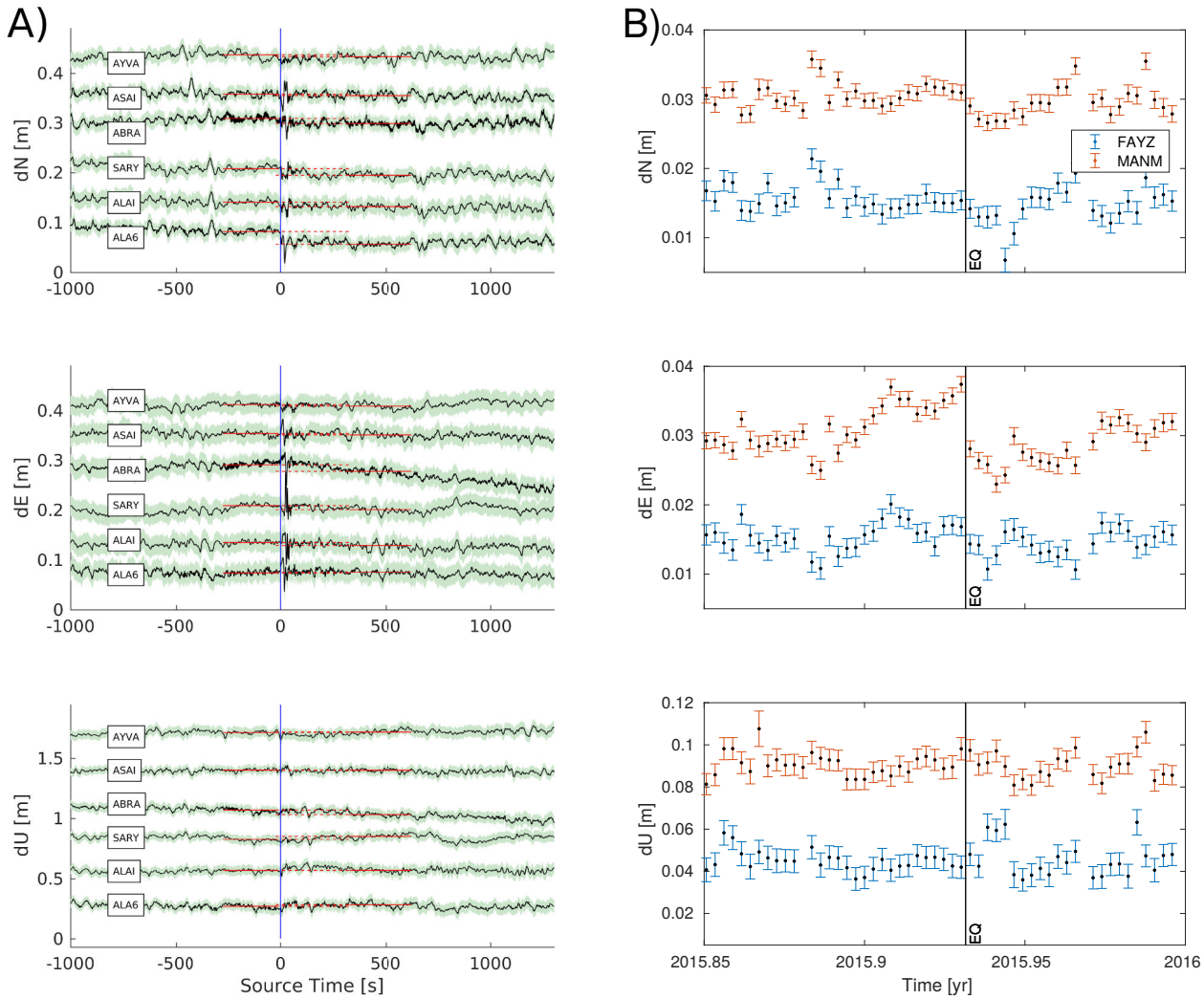

Figure 3. A) The 1 Hz GPS static displacements (uncertainties in bright green) are estimated as the difference of the median (red) before and after the rupture time (blue). B) Daily positions of stations FAYZ and MANM before and after the earthquake (EQ).

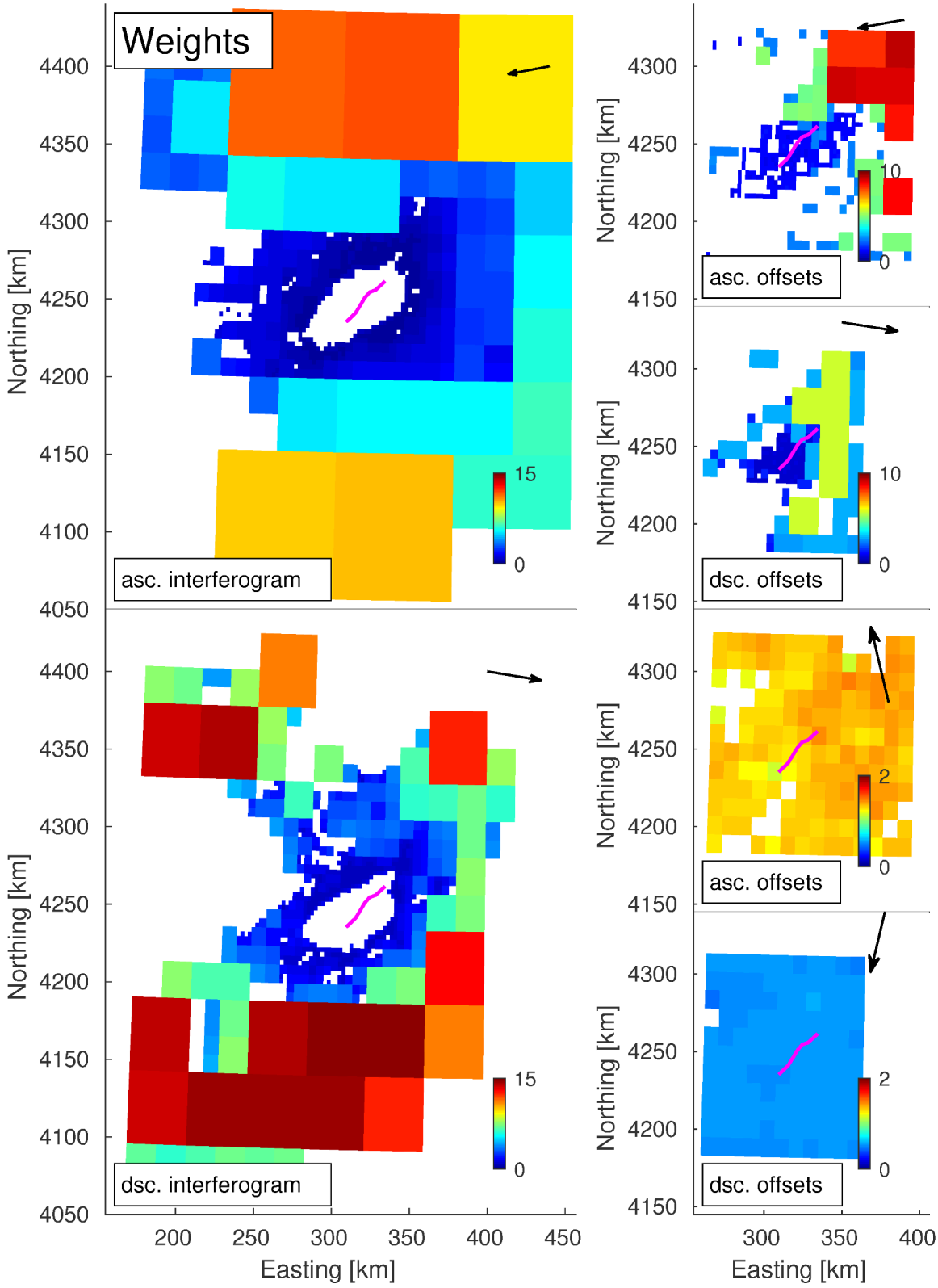

Figure 4. SAR data weights, see Figure S2 for explanation of other features. Note the varying color scales.

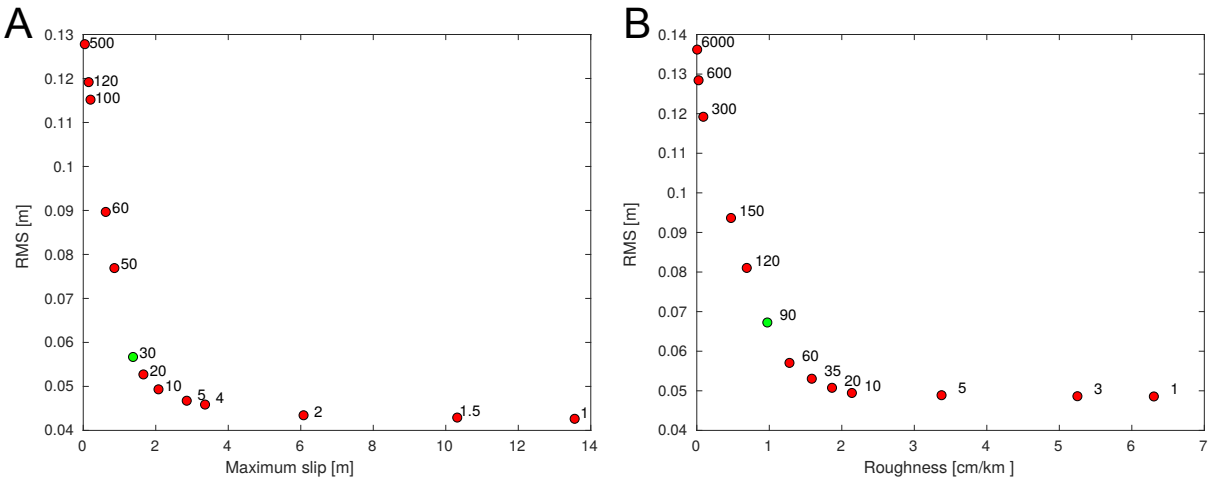

Figure 5. A) The trade-off curve between maximum slip and best-fit (RMS) highlights the best smoothing value (green) used in the optimal-patch model inversion. B) For the uniform-patch model inversion the best smoothing factor is chosen based on the trade-off between the model roughness [*Jónsson et al.*, 2002] and the data fit (RMS).

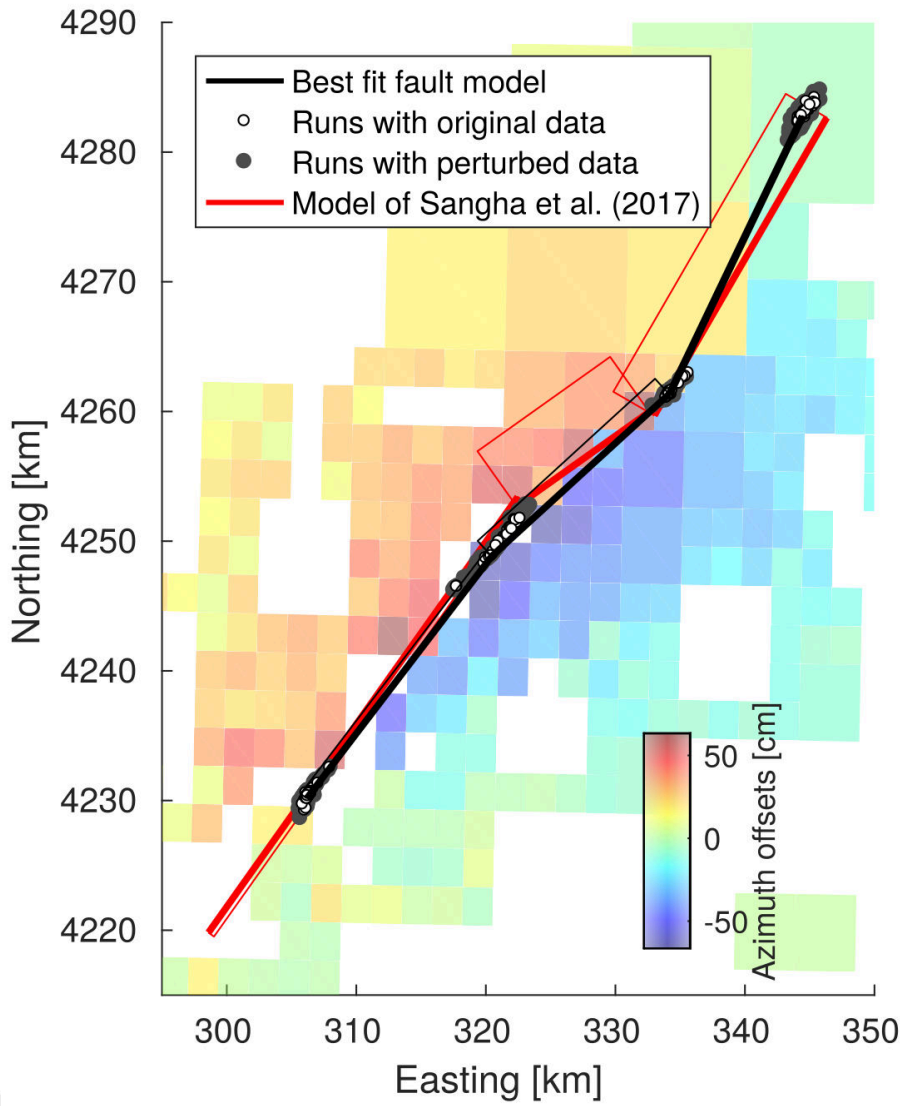

Figure 6. Coordinate constraints of the optimal fault geometry. The best-fit solution is indicated in black and compared to the fault model of *Sangha et al.* [2017] (red). The background is the amplitude pixel offset estimate of the ascending SAR acquisitions.

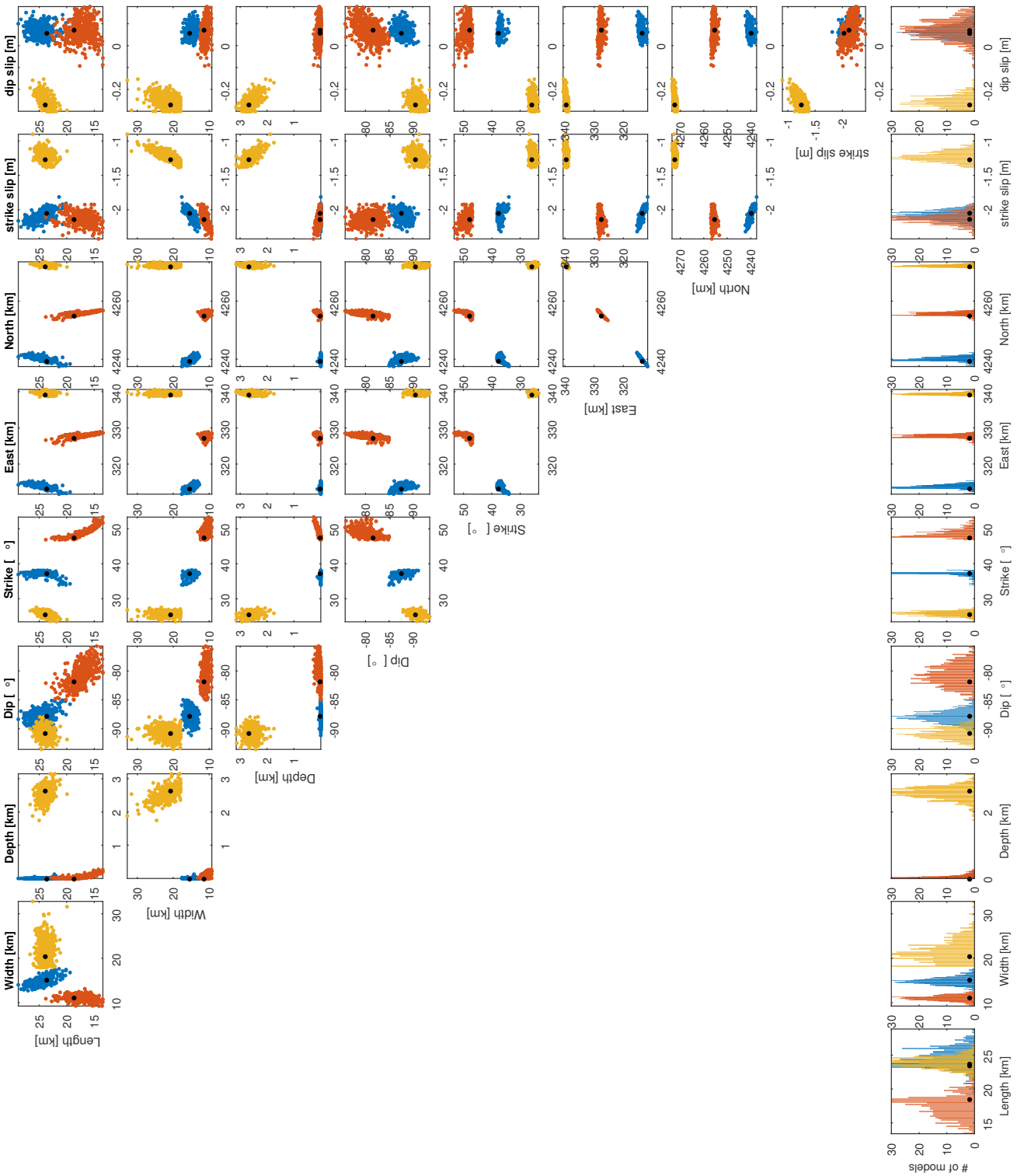

Figure 7. Scatterplots and histograms (bottom line) showing model parameter dependencies and distributions as obtained after 500 optimization runs with perturbed input data. The parameters are color coded by fault segment (blue-orange-yellow from SW to NE, see Figure S6) and the best-fit solution of the unperturbed data is marked with a black dot.

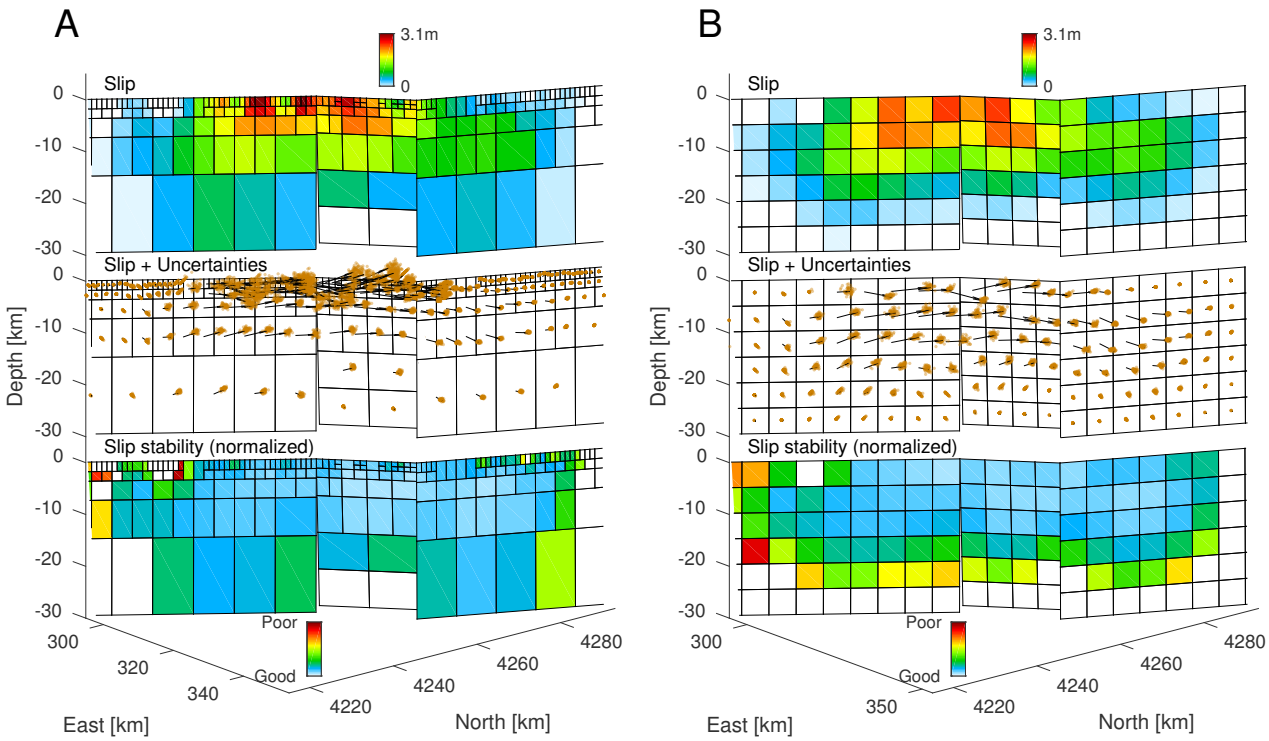

Figure 8. Slip models obtained from the optimal-patch (A) and the uniform patch resolution (B), showing (top to bottom) color-coded slip amplitudes, rake (arrows) with slip uncertainties as orange clouds and the normalized slip stability, i. .e. the standard deviation of the slip parameter uncertainty estimation, normalized by the best-fit slip amplitude of each fault patch.

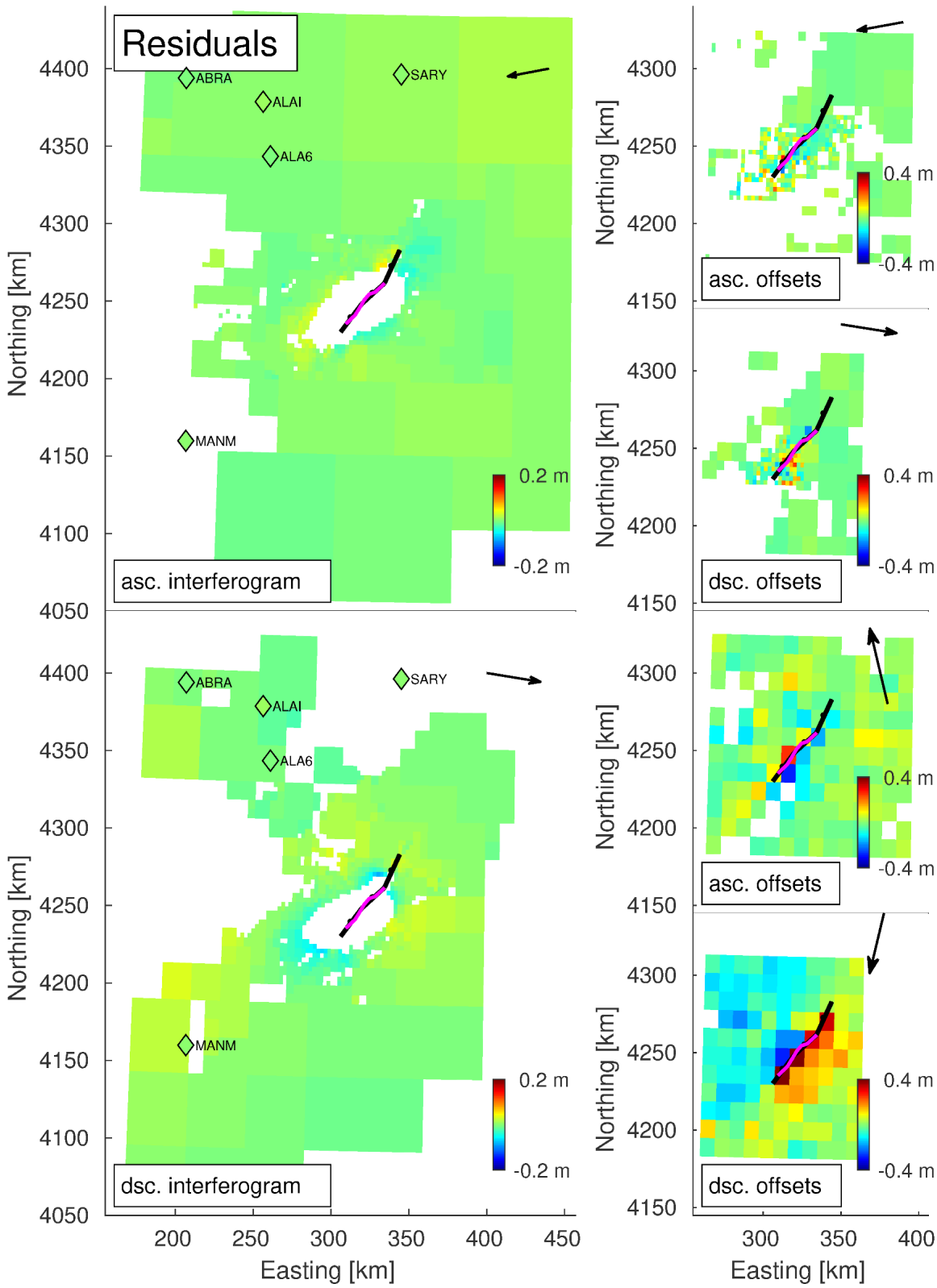

Figure 9. Difference between the best-fit model predictions and observations. The black line outlines the model geometry. See Figure S2 for explanation of other features.

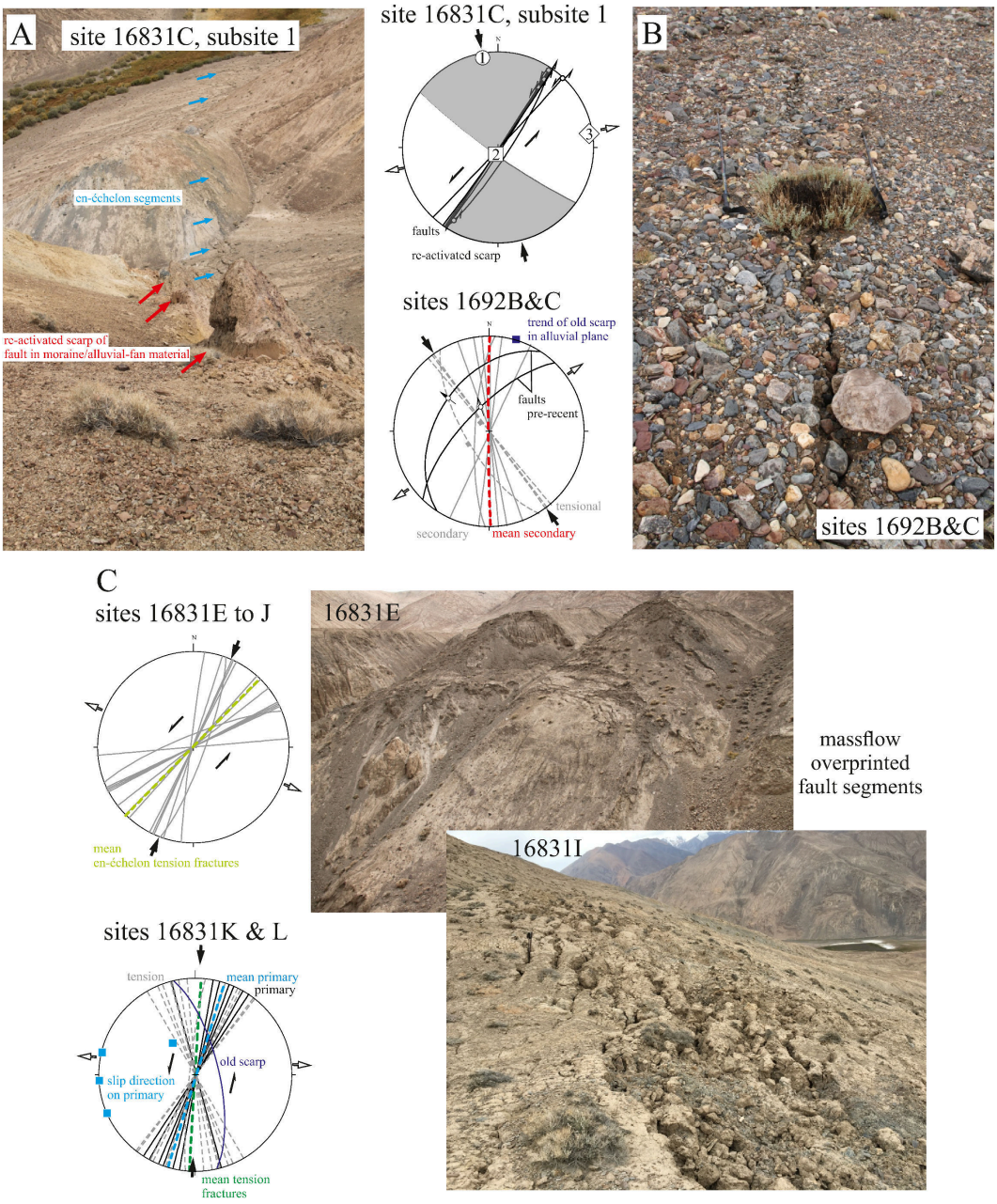

Figure 10. Details of the field observations. See Figure 7B in main text for location. (A) Site 16831C. The surface breaks run up a hillslope and reactivate a pre-existing fault zone that cuts consolidated moraine and alluvial-fan material, forming a scarp. Slickenlines on different faces of the polished master-fault allow the calculation of the reduced stress-tensor (top center), revealing a pure strike-slip solution with a ~35° trending fault plane, similar to the modeled 2015 earthquake rupture. (B) Sites 1692B&C characterize the northernmost surface breaks of the 2015 Sarez earthquake. These comprise a few-m long tension fractures with sinistral strike-slip offset of a few cm in horizontal gravelly riverbank deposits. (C) Sites 16831E to L characterize mass-movement overprinted fault segments. Although these sites show the typical en-échelon arrangement of tensional fractures, however, they are shorter and wider than those on the horizontal sites, and are characteristically downhill-concave.

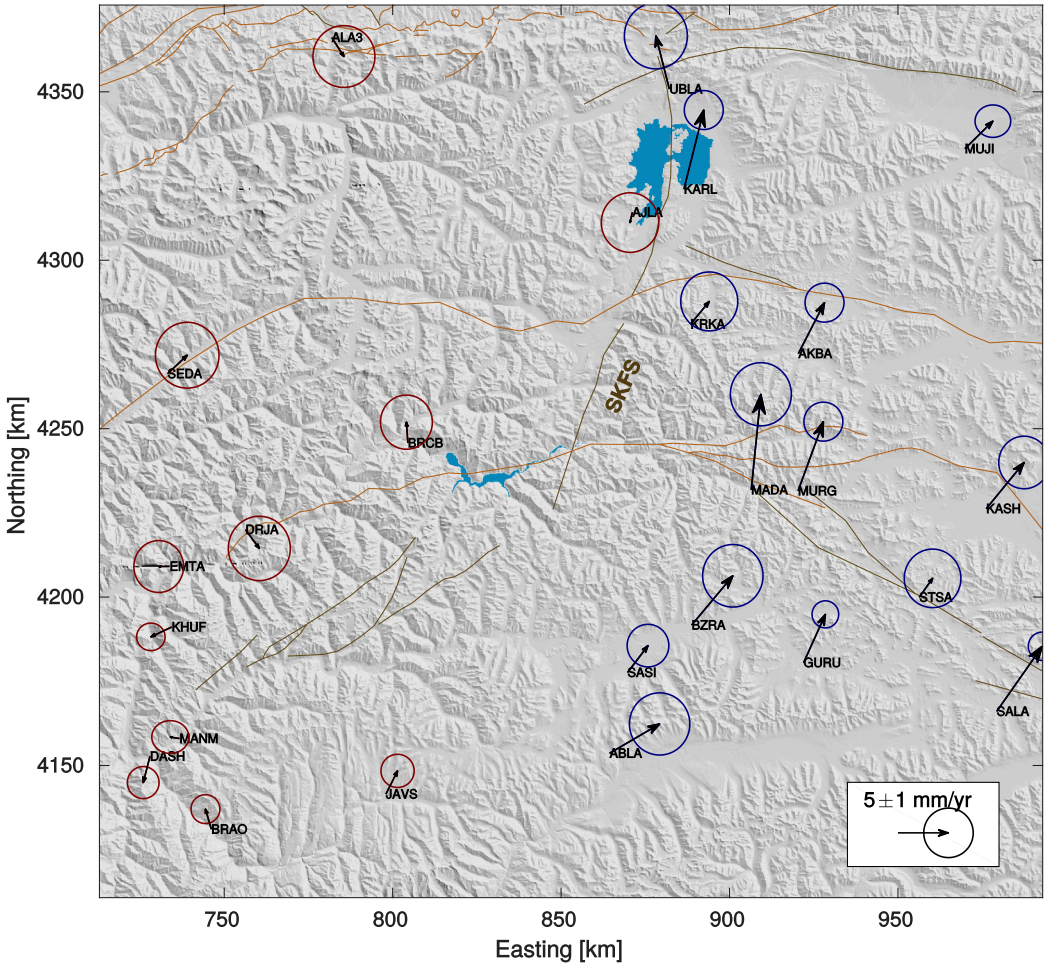

Figure 11. GPS rates (arrows) of the Central Pamir in a reference frame fixed to West Pamir (i. e. the average rate of all stations marked with red uncertainties was subtracted from the original, Eurasian-fixed reference frame). GPS rates of the East Pamir (arrows with blue uncertainties) exhibit an increased NNE motion of 5±2 mm/yr (in average) compared to GPS rates of the West Pamir.